

# Electronic and topological properties of extended two-dimensional Su-Schrieffer-Heeger models and realization of flat edge bands

Hongyu Ma,<sup>1,2,3</sup> Ze Zhang<sup>1,4</sup>, Pei-Hao Fu<sup>1,4</sup>, Jiansheng Wu<sup>1,2,3,\*</sup> and Xiang-Long Yu<sup>1,2,3,†</sup>

<sup>1</sup>Shenzhen Institute for Quantum Science and Engineering, Southern University of Science and Technology, Shenzhen 518055, China

<sup>2</sup>International Quantum Academy, Shenzhen 518048, China

<sup>3</sup>Guangdong Provincial Key Laboratory of Quantum Science and Engineering, Southern University of Science and Technology, Shenzhen 518055, China

<sup>4</sup>Department of Physics, Southern University of Science and Technology, Shenzhen 518055, China



(Received 14 August 2022; accepted 28 November 2022; published 8 December 2022)

One-dimensional Su-Schrieffer-Heeger (SSH) chains are one of the simplest topological models and have been studied extensively. The two-dimensional (2D) version has been confirmed to have a nontrivial topology. In this work, we further extend the 2D SSH model by constructing different configurations, including all possible configurations with 4-site unit cells and another two complicated, but typical, configurations with 8- and 36-site unit cells, respectively. We calculate and analyze the electronic structures and topologies of these SSH models in detail and identify several rich and novel properties, such as topologically protected edge states, metallic chains with different shapes, and a bulk–edge separation in a metal system. In particular, a flat-band feature of topological edge states is obtained. By analyzing the spatial distribution of these edge states, we explain the origin of the flat edge bands and show that bonding squares play a crucial role in the formation of flat bands. Our study can be generalized to more configurations and higher dimensions, providing a basis for further theoretical and experimental explorations.

DOI: [10.1103/PhysRevB.106.245109](https://doi.org/10.1103/PhysRevB.106.245109)

## I. INTRODUCTION

In recent decades, topological band theory has been developed and extended to various systems [1–3], such as topological insulators [4–7], topological crystalline insulators [8,9], and Weyl semimetals [10–12]. In these materials, various topological boundary states arise due to the nontrivial bulk topology. Previous studies have reported that the origin of the nontrivial bulk topology is the nonvanishing Berry curvature [13–16]. The Berry curvature can be viewed as a geometric field strength in momentum space. When its integration over the momentum space generates a nonzero topological invariant, topological boundary states appear in finite-size systems. These states have promising applications in low-power-dissipation information processing and can be used to design electronic and spintronic devices.

The one-dimensional (1D) Su-Schrieffer-Heeger (SSH) model, as one of the simplest topological models, and its extended versions with different interactions have been studied extensively over many decades [17–31]. Several models have been realized in different physical platforms, such as ultracold atoms [26,32,33], quantum circuits [27,28,34], polaritons in an array of micropillars [35], and mechanical granular chains [36]. In recent years, the two-dimensional (2D) SSH model, an extension of the 1D SSH chain, has been intensively investigated and found to exhibit a nontrivial topological phase

and some novel properties, such as fractional wave polarization and high-order topological states [37–43]. Interestingly, different from the abovementioned topological systems, the Berry curvature vanishes in the 2D SSH system due to the coexistence of time-reversal and inversion symmetries, and thus no longer plays a decisive role in the topological properties [39]. This theoretical discovery not only deepens our understanding of the nontrivial topology, but also opens a new avenue of research. However, most previous studies of the 2D SSH model have focused on the case of the highest symmetry (i.e., the  $C_{4v}$  point group symmetry). Actually, different combinations of the 1D SSH chain can be extended to different 2D configurations, only one of which is the extensively studied 2D SSH model. Therefore, this raises the question of whether interesting topological properties can be found in other 2D configurations.

Motivated by this idea, we construct different 2D SSH extended configurations and calculate their electronic and topological properties. We investigate all the configurations with 4-site unit cells and present different phases, including nontrivial and trivial insulators and metals. Additionally, two relatively complicated configurations with 8- and 36-site unit cells are studied in detail. These configurations exhibit rich electronic structures, nontrivial topological properties, and novel flat-band feature of edge states. Analysis of the weight distribution allows us to explain the origin of the flat edge bands, which can be attributed to the existence of bonding squares at the edges. Our study can be extended to more complicated cases, including larger unit cells and higher dimensions, and provides a basis for theoretical and

\*wuj@sustech.edu.cn

†yuxl@sustech.edu.cn

experimental research into novel electronic and topological properties in SSH models.

The remainder of this paper is organized as follows. In Sec. II, we describe the computational approach used in this study. In Sec. III, we calculate electronic and topological properties of different 2D SSH configurations, and present different quantum phases and flat-band features of the edge states. Finally, we discuss the different phases in the case of the 4-site unit cell and the flat bands, and conclude this paper with a brief summary in Sec. IV.

## II. COMPUTATIONAL DETAILS

### A. Hamiltonian

The construction of a 2D SSH model can be implemented by stacking 1D SSH chains along the direction perpendicular to the chain. The interaction between neighboring chains can be varied. To construct the SSH structure, we force it to obey the rule that *in 2D configurations, each chain along the x and y directions must be able to be regarded as a 1D SSH chain*. Therefore, the general Hamiltonian of any 2D SSH model can be written uniformly as

$$H = \sum_{m,n} [(t_x + \delta_x p_{m,n}) a_{m+1,n}^\dagger a_{m,n} + (t_y + \delta_y q_{m,n}) a_{m,n+1}^\dagger a_{m,n}] + \text{H.c.}, \quad (1)$$

where  $a_{m,n}^\dagger$  ( $a_{m,n}$ ) is the creation (annihilation) operator of a spinless electron at site  $(m, n)$ ,  $t_x$  ( $t_y$ ) is the hopping integral along the  $x$  ( $y$ ) direction,  $\delta_x$  ( $\delta_y$ ) is a tunable parameter corresponding to lattice-electron coupling in the  $x$  ( $y$ ) direction, and  $p_{m,n}$  ( $q_{m,n}$ ) reflects the Peierls distortion along the  $x$  ( $y$ ) direction. By varying the values of  $p_{m,n}$  and  $q_{m,n}$ , we can obtain a variety of extended configurations of the 2D SSH model. For simplicity, and to clarify the properties of different configurations, we define  $u = t - \delta$  and  $v = t + \delta$  with  $t_x = t_y = t$  and  $\delta_x = \delta_y = \delta$  in the following calculations.

### B. Configurations with 4-site unit cells

For an initial exploration, we limit the number of sites in a unit cell to four and fix the hopping integrals in each configuration. Under these two limitations, we plot all possible configurations in Fig. 1, where red dotted lines and black solid lines correspond to  $u$  bonds and  $v$  bonds, respectively. There are 16 configurations in total. They are divided into five classifications. The first classification contains two configurations [Figs. 1(a-i) and 1(a-ii)], which are “complementary” with the exchange of  $u$  and  $v$  and have been extensively studied and simulated in different systems [37–46]. The second classification also contains two configurations, as plotted in Figs. 1(b-i) and 1(b-ii). There are two  $u$  bonds and two  $v$  bonds in their unit cells. The two configurations are also “complementary” and rotationally symmetric with respect to each other. The four configurations in the third classification [Fig. 1(c)] satisfy fourfold rotational symmetry and have the same properties. When we set three  $u$  bonds and one  $v$  bond in the unit cell, another four configurations can be obtained as the fourth classification shown in Fig. 1(d). They also present some symmetry relations. For example, the configurations in Figs. 1(d-i)

and 1(d-ii) [and in Figs. 1(d-iii) and 1(d-iv)] are mirror symmetric with respect to each other. At the same time, the four configurations exhibit fourfold rotational symmetry. The four configurations in Fig. 1(e) form the fifth classification and present a “complementary” relation with those in Fig. 1(d), where each unit cell contains one  $u$  bond and three  $v$  bonds. In the following calculations, according to these symmetries, we only calculate the electronic and topological properties of the configurations shown in Figs. 1(a-i), 1(a-ii), 1(b-i), 1(c-i), 1(d-i), and 1(e-i). These are named configurations I–VI, respectively. The properties of the other configurations can be obtained from their symmetry relations.

### C. Zak phase

The Zak phase is a topological invariant that is usually employed to describe the topology in 1D insulating systems [47]. For example, it has been successfully used to characterize linearly conjugated diatomic polymers [48], photonic systems [49–51], acoustic systems [52], cold atom systems [33], quantum circuits [37], and water wave states [53]. For high-dimensional ( $d \geq 2$ ) systems, the topological invariant is the Chern number or  $Z_2$  in general. However, a counterexample is provided by the 2D SSH model in the absence of the Berry curvature, which leads to a vanishing Chern number but still exhibits a nontrivial topological phase. Previous studies report that it is the Berry connection that provides the nontrivial topology, whose integration over the momentum space is the so-called 2D Zak phase [39]. This is given by [47,54,55]

$$\mathbf{Z} = \frac{1}{2\pi} \iint \mathbf{A} dk_x dk_y, \quad (2)$$

where the integral is over the first Brillouin zone,  $\mathbf{A} = \sum_{m=1}^{occ} i \langle \psi_m | \partial_{\mathbf{k}} | \psi_m \rangle$  is the Berry connection,  $occ.$  is the number of occupied energy bands, and  $|\psi_m\rangle$  is the  $m$ th eigenstate of the Hamiltonian.

More generally, when a 2D insulating system has a dihedral point group symmetry, its Hall conductance remains zero, leading to a vanishing Chern number [56]. Fang *et al.* formulated a theory of quantized electric polarization on such insulators. The electric polarization can serve as a complementary quantum number when the Chern number is zero and can be expressed in terms of parities of bands at high-symmetry points. Obana *et al.* further prove that the electric polarization is proportional to the Zak phase [42]. In this work, when the considered insulating system has  $C_2$  symmetry, the calculation of the Zak phase can be simplified using the electric polarization as  $(Z_x, Z_y) = (2\pi P_x, 2\pi P_y)$  [56]. Here,  $P_{x/y}$  is the electric polarization, which can be expressed by

$$P_j = \frac{1}{2} \times \left( -\frac{i}{\pi} \ln \left\{ \frac{\det[\mathcal{B}(K_j)]}{\det[\mathcal{B}(\Gamma)]} \right\} \bmod 2 \right) = \frac{1}{2} \times \left\{ -\frac{i}{\pi} \ln \left[ \prod_{n \in occ.} \frac{\xi_n(K_j)}{\xi_n(\Gamma)} \right] \bmod 2 \right\}, \quad (3)$$

where  $j$  denotes the direction  $x$  or  $y$ ,  $K_j$  is the high-symmetry point  $X$  or  $Y$  in the first Brillouin zone, and  $\mathcal{B}$  is a sewing matrix, which takes the form of the twofold rotation operator  $\hat{C}_2$  for a multiband system. The elements of the sewing matrix can

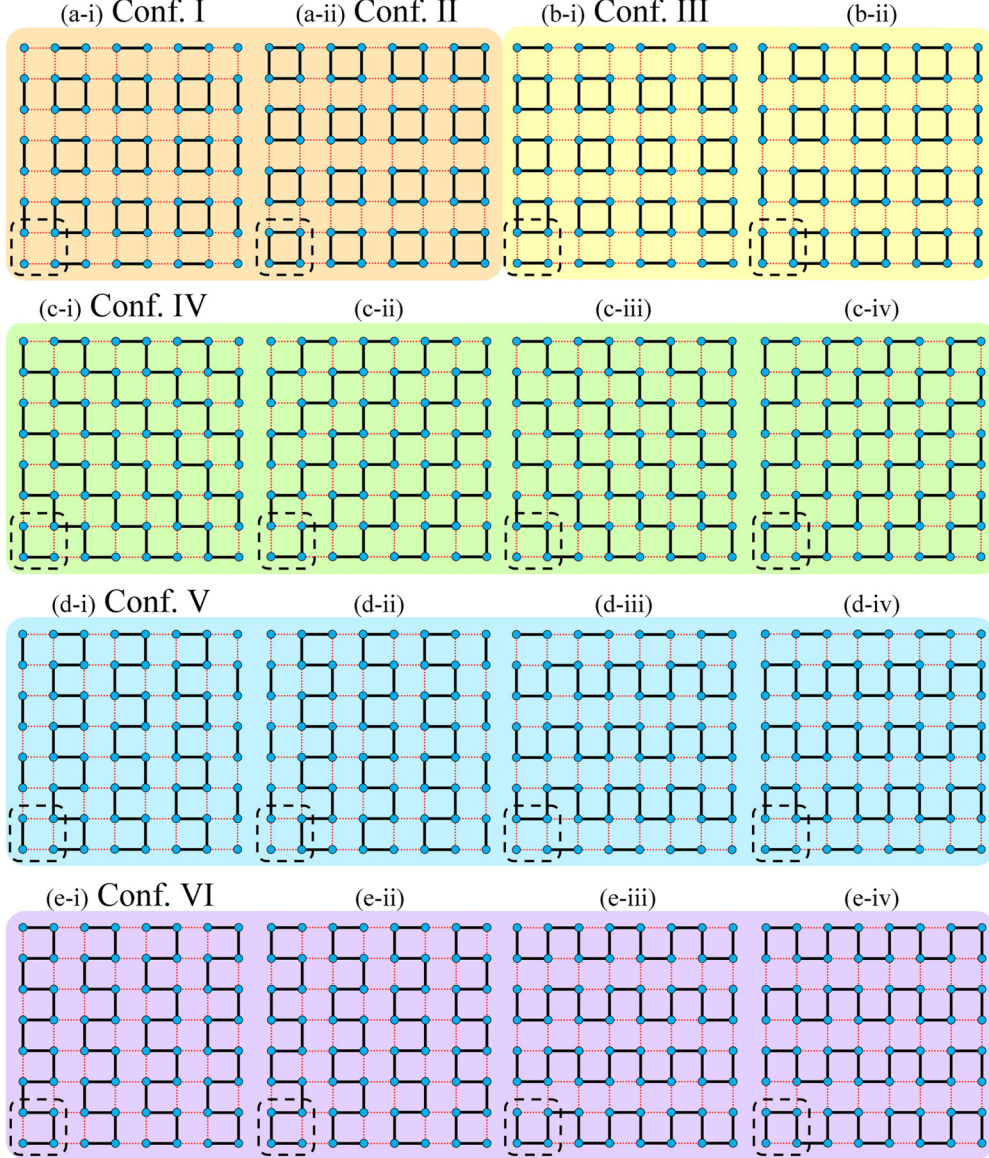


FIG. 1. Sixteen configurations of 2D SSH models with 4-site unit cells. They are divided into five groups with different background colors. Red dotted and black solid lines represent hopping integrals  $u$  and  $v$ . The unit cell in each configuration is marked by a dashed box.

be calculated by  $[B(K_j/\Gamma)]_{pq} = \langle \psi_p(K_j/\Gamma) | \hat{C}_2 | \psi_q(K_j/\Gamma) \rangle$ , where  $p$  and  $q$  run over occupied bands.  $\xi_n(K_j/\Gamma)$  denotes the parity under the  $\hat{C}_2$  operation of the eigenstate at the  $K_j/\Gamma$  point on the  $n$ th band. When a constructed 2D SSH insulating system has a higher symmetry (e.g.,  $C_{2v}$ ,  $C_4$ , and  $C_{4v}$ ), Eq. (3) can be used to calculate the Zak phase, because the three symmetries already imply  $C_2$  [56]. In addition, we find that Eq. (3) is more convenient than Eq. (2) for calculating the Zak phase in systems with larger-size unit cells, such as the 8- and 36-site unit cells considered below.

### III. ELECTRONIC AND TOPOLOGICAL PROPERTIES

Although we have defined the rule for constructing 2D SSH lattices in Sec. II A, there are still countless configurations with increasing unit-cell sizes through different stacking sequences and stacking interactions between the SSH chains. Here, we focus on several typical configurations, including

those with 4-site unit cells, as constructed in Sec. II B, and another two configurations with 8- and 36-site unit cells, respectively. In each case, the Hamiltonian is given by changing  $p_{m,n}$  and  $q_{m,n}$  in Eq. (1). In the following calculations, we set  $u = 1$  and  $v = 4$ , fix the lattice constant to unity, and set the number of unit cells to  $N = 10$  in the open boundary condition, unless stated otherwise. The nanoribbon along the  $x$  ( $y$ ) direction with an open boundary along the  $y$  ( $x$ ) direction is named the  $x$  nanoribbon ( $y$  nanoribbon).

#### A. Configurations I and II

Figures 1(a-i) and 1(a-ii) show configurations I and II, respectively. Their Hamiltonians are given by Eq. (1) through respectively setting

$$p_{m,n} = (-1)^m, q_{m,n} = (-1)^n \quad (4)$$

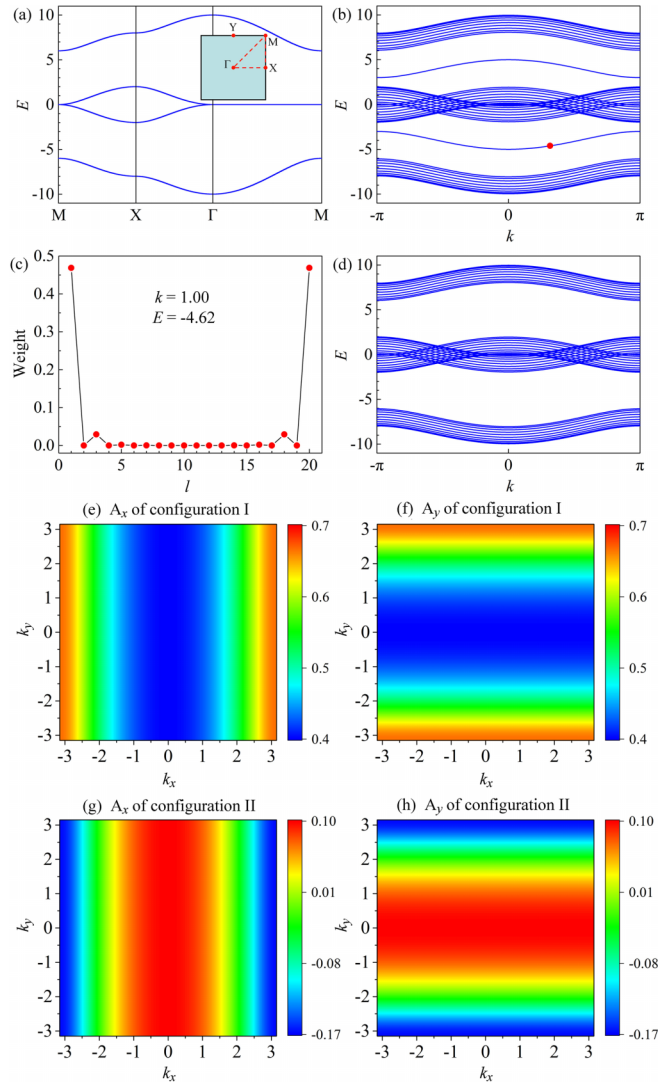


FIG. 2. (a) Bulk band structure of configurations I and II. The inset shows the first Brillouin zone with a high-symmetry path. Nanoribbon band structures of (b) configuration I and (d) configuration II, where  $k = k_x$  or  $k_y$ . (c) Spatial distribution of the state marked by a red point in panel (b).  $l$  is the chain index of a nanoribbon. Berry connections ( $A_x$ ,  $A_y$ ) of (e, f) configuration I and (g, h) configuration II in the first Brillouin zone.

and

$$p_{m,n} = (-1)^{m-1}, q_{m,n} = (-1)^{n-1}. \quad (5)$$

Both configurations have  $C_{4v}$  symmetry. Although their  $u$  and  $v$  bonds are exchanged, they have the same bulk electronic properties, such as the band structure shown in Fig. 2(a). There are four bands and two energy gaps.

The topologies of configurations I and II cannot be characterized by a 2D topological invariant, because both satisfy the time-reversal and inversion symmetries, leading to a vanishing Berry curvature [39]. The Zak phase can be employed for topology characterization. According to Sec. II C, we calculate the Berry connection and the Zak phase. The Berry connections of the two configurations with the lowest band occupied are plotted in Figs. 2(e)–2(h). There are two main

features: (i) the Berry connection  $A_x$  (or  $A_y$ ) is completely independent of  $k_y$  (or  $k_x$ ) and (ii) for configuration I, the Berry connection is always greater than 0, while for configuration II, it can be greater or less than 0 in the Brillouin zone. Further, the Zak phase can be obtained by integrating the Berry connection over the whole Brillouin zone. Its analytic expression is given as

$$Z_x = Z_y = \frac{\pi}{2} - \frac{\pi}{2} \frac{u-v}{|u-v|} = \pi \quad \text{for configuration I,} \quad (6)$$

$$Z_x = Z_y = \frac{\pi}{2} + \frac{\pi}{2} \frac{u-v}{|u-v|} = 0 \quad \text{for configuration II,} \quad (7)$$

corresponding to nontrivial and trivial topologies, respectively.

Figures 2(b) and 2(d) plot the nanoribbon band structures of these two configurations. They are nearly identical, except that there exist particle states within the bulk gap in configuration I. We further investigate the weight distribution of these states in Fig. 2(c), which suggests that they are edge states. This exactly corresponds to the nontrivial Zak phase.

We can use a simple and intuitive picture to understand the nontrivial and trivial topologies. In these two configurations, the four sites connected by the four  $v$  bonds form a bonding square. Such squares cover all of the sites in configuration II and the inner sites of configuration I, but there are no bonding squares at the edges of configuration I. This is also one of the reasons for the formation of edge states within the bulk gap. The bonding squares at the edges suppress the formation of the edge states, corresponding to the trivial topology in configuration II.

## B. Configuration III

When we set

$$p_{m,n} = (-1)^{m-1}, \quad q_{m,n} = (-1)^n \quad (8)$$

in Eq. (1), the Hamiltonian describes configuration III, shown in Fig. 1(b-i). The band calculations show that this configuration has the same bulk band structure as configurations I and II. This is reasonable because all configurations have the same bulk lattice. The difference is their boundaries, leading to different topological properties. The Berry connection of configuration III along the  $x$  (or  $y$ ) direction is identical to that of configuration I (or II), resulting in the Zak phase  $\mathbf{Z} = (\pi, 0)$ . Accordingly, there exist edge states within the bulk gap in an  $x$  nanoribbon, while no such edge states occur in a  $y$  nanoribbon. The corresponding nanoribbon band structures are the same as in Figs. 2(b) and 2(d).

## C. Configuration IV

The Hamiltonian of configuration IV [Fig. 1(c-i)] can be obtained by setting

$$p_{m,n} = (-1)^{m+n}, \quad q_{m,n} = (-1)^{m+n} \quad (9)$$

in Eq. (1). By diagonalizing the Hamiltonian in the momentum space, we obtain the bulk band structure shown in Fig. 3(a). Obviously, this is a metal system and this behavior can be attributed to the 1D metallic chain with  $v$  bonds along the diagonal direction. The nanoribbon band structure

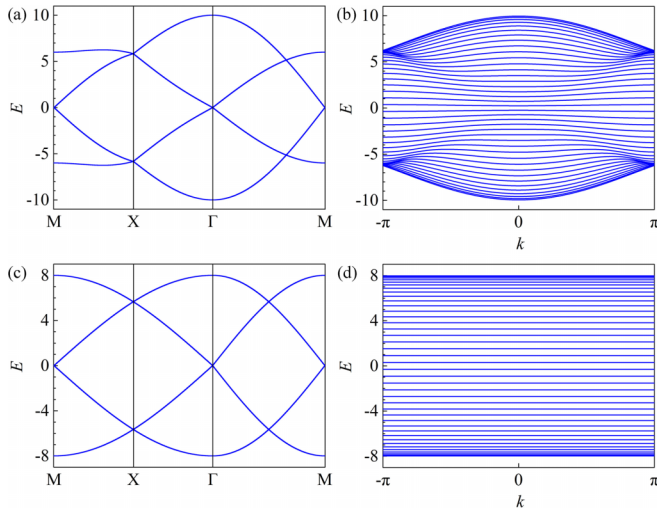


FIG. 3. (a) Bulk and (b) nanoribbon band structures of configuration IV. (c, d) Band structures with another set of parameters,  $u = 0$  and  $v = 4$ .  $k = k_x$  or  $k_y$  in panels (b) and (d).

in Fig. 3(b) also clearly illustrates the metallicity without band gaps. It is worth noting that the bands near the Fermi level show a flat-band feature. Recently, flat-band systems have become a hot topic due to the novel properties induced by different physical mechanisms [57–59]. Physically, the flat-band phenomenon means the particles have zero velocity, corresponding to a locality. We deduce that this comes from the weak hopping integrals of  $u$  bonds between the finite-length metallic chains. To check this, we consider a limiting situation in which  $u = 0$  and  $v = 4$  in an  $x$  or  $y$  nanoribbon, leading to isolated metallic chains with a finite chain length. Particles cannot conduct along the nanoribbon. The calculation results show a totally flat band structure in Fig. 3(d), in spite of the large dispersion of the bulk bands in Fig. 3(c), verifying our deduction.

#### D. Configurations V and VI

When we set

$$p_{m,n} = (-1)^m, \quad q_{m,n} = (-1)^{m+n} \quad (10)$$

and

$$p_{m,n} = (-1)^{m-1}, \quad q_{m,n} = (-1)^{m+n-1} \quad (11)$$

in Eq. (1), the Hamiltonians of configurations V and VI are obtained, respectively. Their lattice structures are plotted in Fig. 1(d-i) and 1(e-i). The two configurations have the same bulk band structures, where the gap around the Fermi level is closed at the  $\Gamma$  point and the other two gaps around  $E = \pm 4.25$  are closed at the  $M$  point. Thus, both systems are metals. However, they present different nanoribbon band structures due to their different edges, as shown in Figs. 4(b)–4(d). There exist two isolated bands in the  $y$  nanoribbon of configuration V. Although submerged in the bulk bands, they can be separated from the others and contributed to by the edge states. This suggests that there exist edge conduction states independent of bulk states. In addition, the  $x$

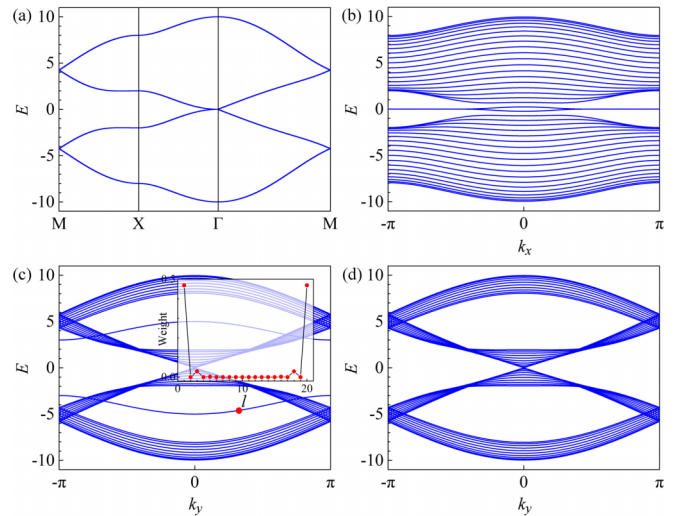


FIG. 4. (a) Bulk and (b)  $x$ -nanoribbon band structures of configurations V and VI.  $y$ -nanoribbon band structures of (c) configuration V and (d) configuration VI. The inset in panel (c) shows the spatial distribution of the state marked by the red point.

nanoribbons of these two configurations have the same band structures due to having the same top and bottom edges.

#### E. Configurations with 8- and 36-site unit cells

Besides the case of the 4-site unit cell, we investigated other configurations with different unit-cell sizes, and found a nontrivial one with an 8-site unit cell. The lattice structure of this configuration is plotted in Fig. 5(a) and the Hamiltonian is given by setting

$$p_{m,n} = (-1)^m, \quad q_{m,n} = \begin{cases} (-1)^{(m-1)/2+n}, & \text{if } m \text{ is odd,} \\ (-1)^{m/2+n}, & \text{if } m \text{ is even,} \end{cases} \quad (12)$$

in Eq. (1). The lattice structure is similar to that of configurations I and II, with bonding squares being formed. The difference is that there is a relative translation between the nearest-neighbor bonding-square columns. By diagonalizing the Hamiltonian, we obtain a bulk band structure with eight bands and two energy gaps, as shown in Fig. 5(b).

A fundamental property of topological insulators is the existence of edge states that are topologically protected. As the lattice structure is anisotropic, we calculate its  $x$  and  $y$  nanoribbons separately. By analyzing the nanoribbon band structures in Figs. 5(c) and 5(d), we find three main features. (i) The number of bands for the  $x$  nanoribbon is twice the number for the  $y$  nanoribbon. This is because the width of the nanoribbon is set to 10 unit cells and each unit cell has four and two lattice sites along the  $x$  and  $y$  directions, respectively. (ii) Two isolated bands within the bulk gaps are contributed to by edge states, as illustrated in the insets of Figs. 5(c) and 5(d). (iii) The bands of the two different nanoribbons present different dispersion degrees. This behavior is apparent in the bulk band structure, where the overall dispersion along the  $k_y$  direction ( $\Gamma - Y$  and  $X - M$ ) is greater than that along the  $k_x$  direction ( $\Gamma - X$  and  $Y - M$ ). Most notably, the edge states

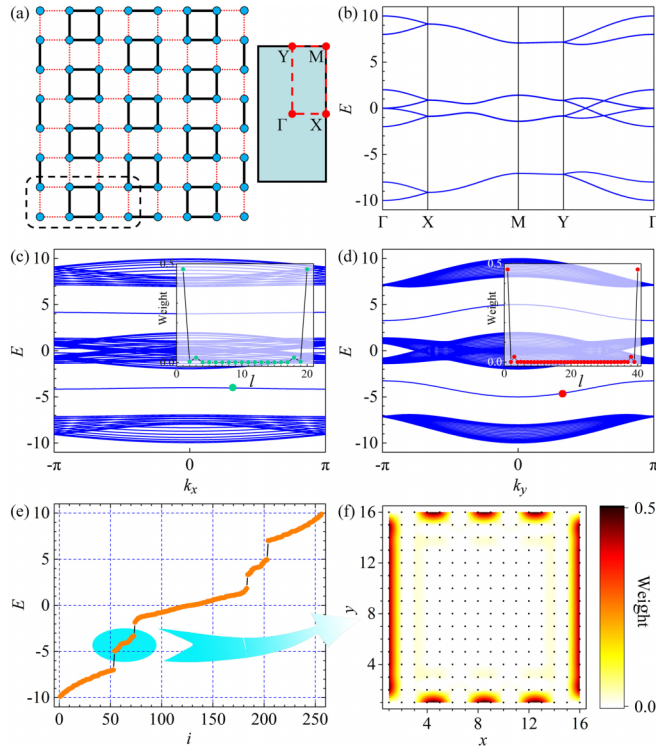


FIG. 5. (a) Configuration with an 8-site unit cell and the corresponding Brillouin zone with a high-symmetry path. (b) Bulk band structure. (c)  $x$ - and (d)  $y$ -nanoribbon band structures. The two insets show the spatial distributions of the states marked by red and green points in the band structures, respectively. (e) Eigenvalues of the finite system with  $16 \times 16$  sites. (f) Spatial distribution of the states in the blue region of panel (e). For an intuitive picture, we interpolated the weights in the interstitial region from those of the nearest-neighbor sites.

of the  $x$  nanoribbon show a nearly flat-band feature compared with those of the  $y$  nanoribbon. This indicates stronger locality at the top and bottom edges. The lattice structure has bonding squares at these two edges, while there are no such squares at the left and right edges. Importantly, the bonding squares are not good for the formation and conduction of the edge states within the bulk gaps, as stated in Sec. III A. Thus, the flat-band feature can be attributed to the existence of bonding squares at the edges. The eigenvalues and distribution of edge states for a finite system are plotted in Figs. 5(e) and 5(f), respectively. The weight on the bonding squares is nearly zero, especially at the edges. Therefore, the bonding squares may hinder the transport of particles at the edges.

To further confirm the above explanation for the flat-band feature of the edge states, we construct a more complicated configuration to realize the flat-band-type edge states at all edges. The Hamiltonian can be obtained by setting

$$p_{m,n} = \begin{cases} (-1)^{\lfloor (n-1)/2 \bmod 3 \rfloor + m - 1}, & \text{if } n \text{ is odd,} \\ (-1)^{\lfloor (n/2-1) \bmod 3 \rfloor + m - 1}, & \text{if } n \text{ is even,} \end{cases} \quad (13)$$

$$q_{m,n} = \begin{cases} (-1)^{\lfloor (m-1)/2 \bmod 3 \rfloor + n - 1}, & \text{if } m \text{ is odd,} \\ (-1)^{\lfloor (m/2-1) \bmod 3 \rfloor + n - 1}, & \text{if } m \text{ is even,} \end{cases} \quad (14)$$

in Eq. (1). The lattice structure is plotted in Fig. 6(a), and there are 36 lattice sites in each unit cell. Bonding squares exist

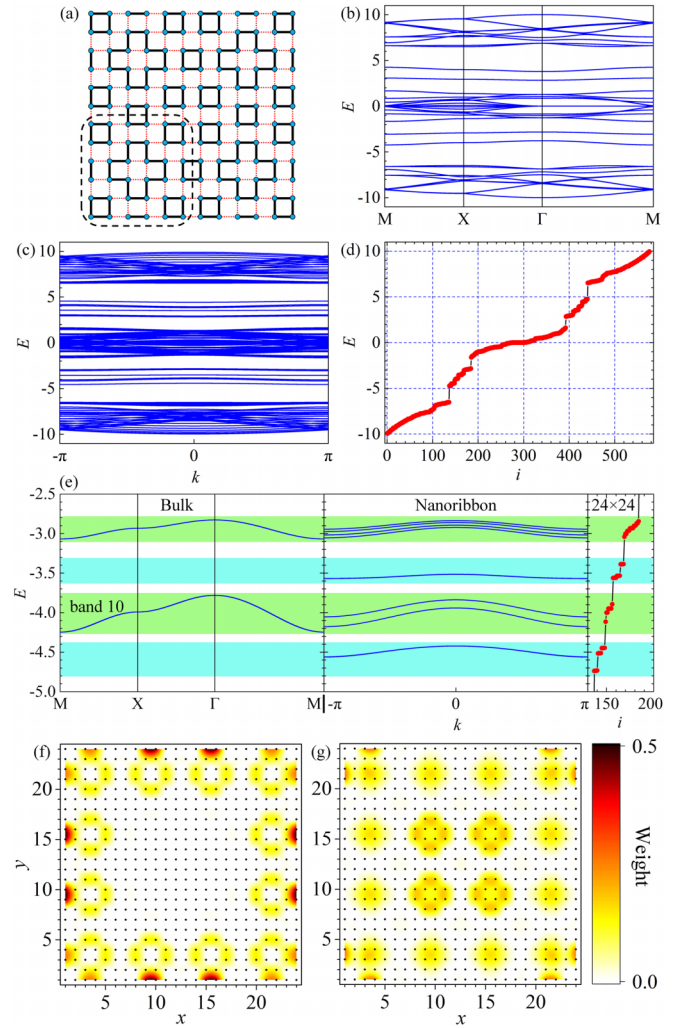


FIG. 6. (a) Configuration with a 36-site unit cell. (b) Bulk band structure. (c) Nanoribbon band structure, where  $k = k_x$  or  $k_y$ . (d) Eigenvalues of the finite system with  $24 \times 24$  sites. (e) Comparison of the band structures in panels (b), (c), and (d) in the range  $E = -5$ – $-2.5$ , where bulk and edge states are marked in green and blue, respectively. (f, g) Spatial distributions of the states in green and blue regions of the rightmost panel of (e), respectively.

at the edges. Based on the above results, we expect localized edge states with the flat-band feature to appear within the bulk gap. To verify this, we first calculate the band structures. In Fig. 6(b), the bulk bands can be separated into five groups. In the ranges  $E = -10$ – $-6$ ,  $-2$ – $2$ , and  $6$ – $10$ , the bands have a relatively large degree of dispersion. In the ranges  $E = -5$ – $-3$  and  $3$ – $5$ , there are two nearly flat bands. We further plot the nanoribbon band structure and find another two flatter bands in these ranges [Fig. 6(c)], which are contributed to by the edge states. To intuitively present the localization of the edge states, we calculate a finite system and plot its eigenvalues in Fig. 6(d). By comparing these with the nanoribbon and bulk band structures in Fig. 6(e), it appears that the states marked by the blue background correspond to the two flat bands in the nanoribbon structure, suggesting that these are edge states. The weight distributions of the energy states on the lattice structure are plotted in Figs. 6(f) and 6(g), which

TABLE I. Parities of the eigenstates at the  $\Gamma$ ,  $X$ , and  $Y$  points for the lowest ten bands of the configuration with the 36-site unit cell.  $j$  is the band index.

$j$	1	2	3	4	5	6	7	8	9	10
$\xi_j(\Gamma)$	+	+	-	-	+	+	+	-	-	+
$\xi_j(X/Y)$	+	-	+	-	+	-	+	-	-	+

further illustrates that they are from the four edges. Moreover, they are separated by the bonding squares and are discretely distributed at the edges. This results in the localization of particles, self-consistently corresponding to the flat-band feature.

To further determine the nontrivial topology of the two configurations, we calculated their topological invariants. As their unit cells have  $C_{2v}$  and  $C_{4v}$  symmetries, respectively, Eq. (3) can be used to calculate their Zak phases. For the case of the 8-site unit cell, the parity  $\xi_n(X/Y)$  cannot be obtained directly, because at the  $X$  and  $Y$  points the two occupied bands with opposite parities are degenerate. But we can calculate the Zak phase by using the first line of Eq. (3), where  $\det[\mathcal{B}(\Gamma)] = 1$  and  $\det[\mathcal{B}(X)] = \det[\mathcal{B}(Y)] = -1$ . This leads to a nonzero Zak phase  $\mathbf{Z} = (\pi, \pi)$ , corresponding to a nontrivial topology. For the case of the 36-site unit cell, we calculate the parities at  $\Gamma$ ,  $X$ , and  $Y$  points and show the calculation results of the lowest ten bands in Table I. When the number of occupied bands is nine and ten [band 10 is marked in Fig. 6(e)], both Zak phases are  $(\pi, \pi)$ . Therefore, the calculations of edge states and Zak phases in the two complicated configurations are in exact agreement with each other.

#### IV. DISCUSSION AND CONCLUSION

We have extended previous studies of the 2D SSH model that focused on configurations I and II. By investigating the 16 configurations with different 4-site unit cells, we found four insulating systems and twelve metallic systems. For the four insulators, three of them (configurations I and III) are nontrivial with topological edge states and the other one (configuration II) is trivial. For the twelve metals, their metallicity can be attributed to the formation of metallic chains with  $v$  bonds. In configuration IV, the metallic chain runs along the diagonal direction and has a zigzag shape. In configurations V and VI, the chain is oriented along the  $x$  or  $y$  direction and has an ‘‘S’’ shape. Notably, configuration V presents a novel phenomenon, where the edge states are in the energy range of bulk states, but can be independent, as shown in Fig. 4(c). This is unexpected in a metallic system and corresponds to bulk–edge separation.

For two other, more complicated configurations, we identified an interesting flat-band feature of the edge states. In the case of the 8-site unit cell, flat bands form at the top and bottom edges. In the case of the 36-site unit cell, they are realized at all four edges. Recently, systems with flat bands have attracted considerable interest due to their novel and unusual properties, and they provide an excellent platform for the study of quantum phases [57–59]. Their flat-band behaviors can be attributed to different physical mechanisms, including symmetry [60,61], nontrivial topology [62–65], and

interactions [66–71]. In particular, the interactions in the flat-band systems lead to rich and interesting phenomena, such as disorder-free many-body localization [72–75], ferromagnetism [76–82], superfluidity [83–85], superconductivity [86], and pair formation for hard-core bosons [87]. However, the underlying physics in our considered systems are somewhat different. In our case, the bonding squares at the edges prevent particle conduction, resulting in the flat band. In addition, configuration IV exhibits flat bands in nanoribbons, as shown in Figs. 3(b) and 3(d). However, different from all of the above physical mechanisms, this is caused by the weak interaction between metallic chains and the finite length of the diagonal metallic chains in the  $x$  and  $y$  nanoribbons.

We compared the bonding square with analogous states or orders in other systems and found some common features. First, this square is similar to the plaquette formed by valence bonds in a  $S = 1/2$  Heisenberg model [88,89]. Both structures have a closed loop, resulting in the localization of particles. Comparing the bonding square with the bond of a large hopping integral in a 1D SSH chain, the common feature is that both are unfavorable for the formation of edge states. The only difference is the dimension, with the 1D edge bands becoming 0D edge levels when moving from the 2D model to the 1D model. According to this comparison, we predict that there exists a bonding cube in a 3D SSH model, which may lead to 2D flat bands at the boundaries.

One may wonder whether other loops play the same role as the bonding square in producing the flat edge bands. Our answer is no. In the 2D SSH model, the smallest loop is the bonding square and the second-smallest loop is a cross-shaped structure called a bonding cross, as presented in Fig. 6(a). We investigated the case in which the bonding crosses are at the edges, and found that they are not conducive to the formation of the flat edge band, but promote the itinerancy of particles. Detailed calculation results are given in the Supplemental Material [90] (see also Refs. [91–95] and references therein). When a larger loop is considered, one can naturally deduce that the itinerancy and delocalization will be further enhanced. Therefore, other loops except the bonding square cannot realize a flat edge band.

For the constructed 2D SSH configurations, we find that all the nontrivial edge states of nanoribbons are doubly degenerate. Their corresponding two eigenwave functions are symmetric and antisymmetric along the width direction, respectively. This topological degeneracy can be attributed to the inversion symmetry of 2D SSH configurations [39].

Another important issue is whether the edge states observed here are just trivial extensions of the edge states of 1D SSH chains. From the above results, such as nanoribbon band structures and edge-state distributions of configuration I, configuration V, and two configurations with 8- and 36-site unit cells, it indeed seems that the edge states of 2D SSH configurations only appear at the ends of nontrivial 1D SSH chains. However, we find that the edge states and topology of our constructed 2D SSH models under the rule stated in Sec. II A cannot be simply predicted from 1D ones. To illustrate this point, we show three specific examples. (i) If we regard the configuration I as an extension of 1D SSH chains, then there should exist nontrivial edge/corner states at four corner sites. However, our study of its finite system reveals

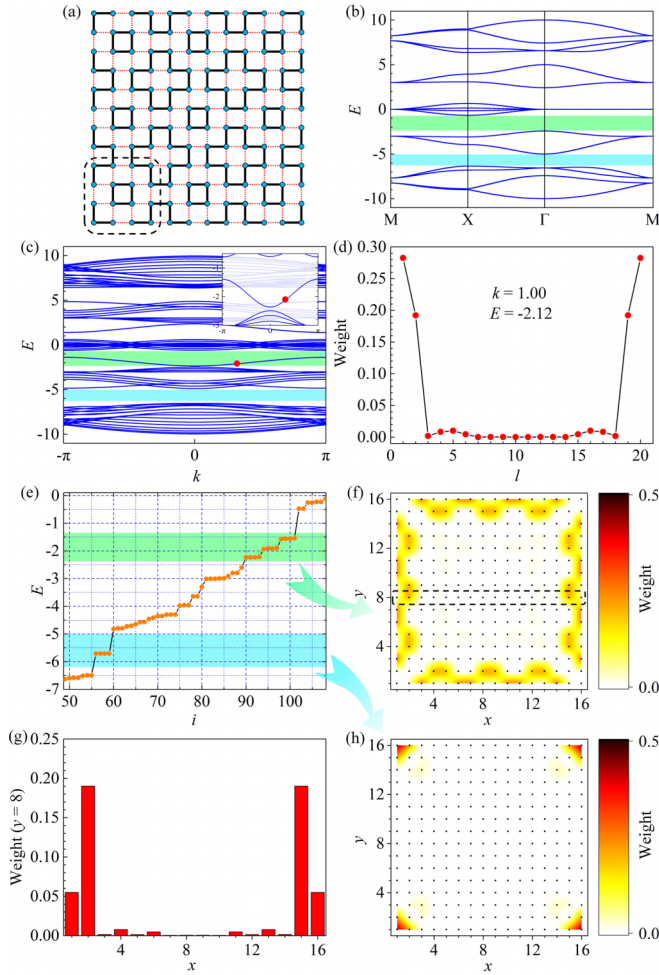


FIG. 7. (a) Configuration with a 16-site unit cell. (b) Bulk band structure. (c) Nanoribbon band structure, where  $k = k_x$  or  $k_y$ . Inset: zoom in of the band structure. (d) Spatial distribution of the states marked by a red point in panel (c). (e) Eigenvalues of the finite system with  $16 \times 16$  sites. (f, h) Spatial distributions of the states in green and blue regions of panel (e), respectively. (g) Spatial distribution with  $y = 8$  marked by dashed box in panel (f).

that none of such states appear within its bulk gap. This phenomenon is also determined in a topological circuit [37]. Previous studies by Xie *et al.* show that the corner states can appear only in a combined structure of trivial and nontrivial configurations [38,41]. (ii) There is a similar behavior in the configuration with a 8-site unit cell [Fig. 5(a)]. According to the topology of 1D SSH chains, edge/corner states should also appear within the bulk gap at four corner sites. However, we do not observe the nontrivial edge/corner states in Fig. 5(f). (iii) We also consider a new configuration with a 16-site unit cell to show that a large hopping strength at the end of a SSH chain may not hinder the edge states in a 2D SSH lattice. The corresponding lattice structure is plotted in Fig. 7(a). We first calculate the bulk band structure and investigate parities at high-symmetry points. The parities at  $\Gamma$ ,  $X$ , and  $Y$  points for the lowest six bands are listed in Table II. When the number of occupied bands is four and six, both Zak phases are  $(\pi, \pi)$ , corresponding to nontrivial topology. The nanoribbon band structure shows that two degenerate bands appear within the

TABLE II. Parities of the eigenstates at the  $\Gamma$ ,  $X$ , and  $Y$  points for the lowest ten bands of the configuration with the 16-site unit cell.

$j$	1	2	3	4	5	6
$\xi_j(\Gamma)$	+	+	-	-	+	+
$\xi_j(X/Y)$	-	+	+	+	-	-

bulk gap around  $E = -2$  in Fig. 7(c). We further calculate its finite system and plot energy levels and spatial distributions of the states within the bulk gap in Figs. 7(e) and 7(f). One can see that all of these states distribute at edges. In particular, the edge states also distribute at the ends with large hopping strength of a trivial SSH chain, as shown in Fig. 7(g). Obviously, the result is not a simple extension of the 1D SSH chain. In addition, we obtain corner states within the bulk gap around  $E = -5.5$ . Remarkably, they distribute at the end of trivial SSH chains. Therefore, the appearance of edge and corner states in 2D SSH systems do not depend entirely on the configuration and topology of the 1D SSH chains. The coupling interaction between chains also plays a crucial role for the topology of the 2D SSH systems. From the above three specific example, we can conclude that 2D SSH configurations constructed under our rule are not trivial extensions of 1D SSH chains and the edge and corner states can be beyond the understanding based on the edge states of 1D SSH chains.

These topologically protected conducting edge states, corner states, flat bands, and the switch between them may be valuable for optical couplers, robust waveguides, and topological circuit switches. According to previous successful simulations of configurations I and II in microwave systems [46], acoustic systems [43,44], and electrical circuits [37,45], it is expected that such exotic properties can be experimentally realized. The relevant parameters may need to be modified from our theoretical calculations, but the topological properties will remain the same.

In summary, we have studied different configurations of the 2D SSH model under the rule stated in Sec. II A, including all the configurations with the 4-site unit cell and two relatively complicated configurations with 8- and 36-site unit cells. Different quantum phases were obtained, e.g., topologically nontrivial and trivial insulators and metals. We investigated their electronic and topological properties in detail, and obtained topologically protected edge states, metallic chains with different shapes, and a bulk-edge separation in a metal system. In particular, a flat-band feature of topological edge states has been presented. We uncovered the physical mechanism of its formation by analyzing the spatial distribution of edge states and the bulk topology. This work can be generalized to more configurations and higher dimensions, and we hope it will provide new ideas for future experimental simulations and observations.

## ACKNOWLEDGMENTS

This work is supported by Science, Technology and Innovation Commission of Shenzhen Municipality (Grants No. JCYJ20190809120203655,

No. ZDSYS20170303165926217, No. JCYJ20170412152620376, and No. KYT-DPT20181011104202253), National Natural Science Foundation of China (Grant No. U1801661), Guangdong

Innovative and Entrepreneurial Research Team Program (Grant No. 2016ZT06D348), and Natural Science Foundation of Guangdong Province (Grants No. 2017B030308003 and No. 2019B121203002).

- [1] M. Z. Hasan and C. L. Kane, *Rev. Mod. Phys.* **82**, 3045 (2010).
- [2] A. Bansil, H. Lin, and T. Das, *Rev. Mod. Phys.* **88**, 021004 (2016).
- [3] X.-L. Qi and S.-C. Zhang, *Rev. Mod. Phys.* **83**, 1057 (2011).
- [4] C. L. Kane and E. J. Mele, *Phys. Rev. Lett.* **95**, 226801 (2005).
- [5] L. Fu, C. L. Kane, and E. J. Mele, *Phys. Rev. Lett.* **98**, 106803 (2007).
- [6] Y. L. Chen, J. G. Analytis, J.-H. Chu, Z. K. Liu, S.-K. Mo, X. L. Qi, H. J. Zhang, D. H. Lu, X. Dai, Z. Fang, S. C. Zhang, I. R. Fisher, Z. Hussain, and Z.-X. Shen, *Science* **325**, 178 (2009).
- [7] C.-Z. Chang, J. Zhang, X. Feng, J. Shen, Z. Zhang, M. Guo, K. Li, Y. Ou, P. Wei, L.-L. Wang *et al.*, *Science* **340**, 167 (2013).
- [8] L. Fu, *Phys. Rev. Lett.* **106**, 106802 (2011).
- [9] Y. Ando and L. Fu, *Annu. Rev. Condens. Matter Phys.* **6**, 361 (2015).
- [10] X. Wan, A. M. Turner, A. Vishwanath, and S. Y. Savrasov, *Phys. Rev. B* **83**, 205101 (2011).
- [11] A. A. Burkov and L. Balents, *Phys. Rev. Lett.* **107**, 127205 (2011).
- [12] H. Watanabe, H. C. Po, M. P. Zaletel, and A. Vishwanath, *Phys. Rev. Lett.* **117**, 096404 (2016).
- [13] X.-L. Qi, and T. L. Hughes, and S.-C. Zhang, *Phys. Rev. B* **78**, 195424 (2008).
- [14] D. N. Sheng, Z. Y. Weng, L. Sheng, and F. D. M. Haldane, *Phys. Rev. Lett.* **97**, 036808 (2006).
- [15] K. Shiozaki and M. Sato, *Phys. Rev. B* **90**, 165114 (2014).
- [16] X.-Y. Dong and C.-X. Liu, *Phys. Rev. B* **93**, 045429 (2016).
- [17] X.-L. Yu, L. Jiang, Y.-M. Quan, T. Wu, Y. Chen, L.-J. Zou, and J. Wu, *Phys. Rev. B* **101**, 045422 (2020).
- [18] W. P. Su, J. R. Schrieffer, and A. J. Heeger, *Phys. Rev. B* **22**, 2099 (1980).
- [19] J. E. Hirsch, *Phys. Rev. Lett.* **51**, 296 (1983).
- [20] J. Voit, *Phys. Rev. Lett.* **64**, 323 (1990).
- [21] M. Rateitzak and T. Koslowski, *Chem. Phys. Lett.* **377**, 455 (2003).
- [22] T. Miyao, *J. Stat. Phys.* **149**, 519 (2012).
- [23] D. Sticlet, L. Seabra, F. Pollmann, and J. Cayssol, *Phys. Rev. B* **89**, 115430 (2014).
- [24] J. Sirker, L. Seabra, F. Pollmann, and J. Cayssol, *J. Stat. Mech.* (2014) P10032.
- [25] M. Weber, F. F. Assaad, and M. Hohenadler, *Phys. Rev. B* **91**, 245147 (2015).
- [26] E. J. Meier, F. A. An, and B. Gadway, *Nat. Commun.* **7**, 13986 (2016).
- [27] C. H. Lee, S. Imhof, C. Berger, F. Bayer, J. Brehm, L. W. Molenkamp, T. Kiessling, and R. Thomale, *Commun. Phys.* **1**, 39 (2018).
- [28] W. Cai, J. Han, F. Mei, Y. Xu, Y. Ma, X. Li, H. Wang, Y. P. Song, Z.-Y. Xue, Z.-Q. Yin, S. Jia, and L. Sun, *Phys. Rev. Lett.* **123**, 080501 (2019).
- [29] M. Ezawa, *Phys. Rev. B* **96**, 121105(R) (2017).
- [30] L. Barbiero, L. Santos, and N. Goldman, *Phys. Rev. B* **97**, 201115(R) (2018).
- [31] Y. Wang, J.-J. Miao, H.-K. Jin, and S. Chen, *Phys. Rev. B* **96**, 205428 (2017).
- [32] S. de Léséleuc, V. Lienhard, P. Scholl, D. Barredo, S. Weber, N. Lang, H. P. Büchler, T. Lahaye, and A. Browaeys, *Science* **365**, 775 (2019).
- [33] M. Atala, M. Aidelsburger, J. T. Barreiro, D. Abanin, T. Kitagawa, E. Demler, and I. Bloch, *Nat. Phys.* **9**, 795 (2013).
- [34] B. Murta, G. Catarina, and J. Fernández-Rossier, *Phys. Rev. A* **101**, 020302(R) (2020).
- [35] P. St-Jean, V. Goblot, E. Galopin, A. Lemaître, T. Ozawa, L. L. Gratiet, I. Sagnes, J. Bloch, and A. Amo, *Nat. Photonics* **11**, 651 (2017).
- [36] R. Chaunsali, E. Kim, A. Thakkar, P. G. Kevrekidis, and J. Yang, *Phys. Rev. Lett.* **119**, 024301 (2017).
- [37] S. Liu, W. Gao, Q. Zhang, S. Ma, L. Zhang, C. Liu, Y. J. Xiang, T. J. Cui, and S. Zhang, *Research* **2019**, 8609875 (2019).
- [38] B.-Y. Xie, G.-X. Su, H.-F. Wang, H. Su, X.-P. Shen, P. Zhan, M.-H. Lu, Z.-L. Wang, and Y.-F. Chen, *Phys. Rev. Lett.* **122**, 233903 (2019).
- [39] F. Liu and K. Wakabayashi, *Phys. Rev. Lett.* **118**, 076803 (2017).
- [40] F. Liu, H.-Y. Deng, and K. Wakabayashi, *Phys. Rev. B* **97**, 035442 (2018).
- [41] B.-Y. Xie, H.-F. Wang, H.-X. Wang, X.-Y. Zhu, J.-H. Jiang, M.-H. Lu, and Y.-F. Chen, *Phys. Rev. B* **98**, 205147 (2018).
- [42] D. Obana, F. Liu, and K. Wakabayashi, *Phys. Rev. B* **100**, 075437 (2019).
- [43] L.-Y. Zheng, V. Achilleos, O. Richoux, G. Theocharis, and V. Pagneux, *Phys. Rev. Appl.* **12**, 034014 (2019).
- [44] Z. Zhang, H. Long, C. Liu, C. Shao, Y. Cheng, X. Liu, and J. Christensen, *Adv. Mater.* **31**, 1904682 (2019).
- [45] N. A. Olekhno, A. D. Rozenblit, V. I. Kachin, A. A. Dmitriev, O. I. Burmistrov, P. S. Seregin, D. V. Zhirihin, and M. A. Gorlach, *Phys. Rev. B* **105**, L081107 (2022).
- [46] X.-D. Chen, W.-M. Deng, F.-L. Shi, F.-L. Zhao, M. Chen, and J.-W. Dong, *Phys. Rev. Lett.* **122**, 233902 (2019).
- [47] J. Zak, *Phys. Rev. Lett.* **62**, 2747 (1989).
- [48] M. J. Rice and E. J. Mele, *Phys. Rev. Lett.* **49**, 1455 (1982).
- [49] S. Longhi, *Opt. Lett.* **38**, 3716 (2013).
- [50] W. Tan, Y. Sun, H. Chen, and S. Q. Shen, *Sci. Rep.* **4**, 3842 (2014).
- [51] F. Cardano, A. D’Errico, A. Dauphin, M. Maffei, B. Piccirillo, C. de Lisi, G. D. Filippis, V. Cataudella, E. Santamoto, L. Marrucci, M. Lewenstein, and P. Massignan, *Nat. Commun.* **8**, 15516 (2017).
- [52] M. Xiao, G. Ma, Z. Yang, P. Sheng, Z. Zhang, and C. Chan, *Nat. Phys.* **11**, 240 (2015).
- [53] Z. Yang, F. Gao, and B. Zhang, *Sci. Rep.* **6**, 29202 (2016).
- [54] R. D. King-Smith and D. Vanderbilt, *Phys. Rev. B* **47**, 1651 (1993).
- [55] R. Resta, *Rev. Mod. Phys.* **66**, 899 (1994).
- [56] C. Fang, M. J. Gilbert, and B. A. Bernevig, *Phys. Rev. B* **86**, 115112 (2012).

- [57] O. Derzhko, J. Richter, and M. Zaksyenko, *Int. J. Mod. Phys. B* **29**, 1530007 (2015).
- [58] D. Leykam, A. Andreanov, and S. Flach, *Adv. Phys.: X* **3**, 1473052 (2018).
- [59] W. Maimaiti, A. Andreanov, and S. Flach, *Phys. Rev. B* **103**, 165116 (2021).
- [60] E. H. Lieb, *Phys. Rev. Lett.* **62**, 1201 (1989).
- [61] R. Bistritzer and A. H. MacDonald, *Proc. Natl. Acad. Sci. USA* **108**, 12233 (2011).
- [62] T. T. Heikkilä and G. E. Volovik, Flat bands as a route to high-temperature superconductivity in graphite, in *Basic Physics of Functionalized Graphite* (Springer, Berlin, 2016), pp. 123–143.
- [63] T. T. Heikkilä, N. B. Kopnin, and G. E. Volovik, *JETP Lett.* **94**, 233 (2011).
- [64] T. Hyart, R. Ojajärvi, and T. T. Heikkilä, *J. Low Temp. Phys.* **191**, 35 (2018).
- [65] H. K. Pal, S. Spitz, and M. Kindermann, *Phys. Rev. Lett.* **123**, 186402 (2019).
- [66] V. A. Khodel and V. R. Shaginyan, *JETP Lett.* **51**, 553 (1990).
- [67] G. E. Volovik, *JETP Lett.* **53**, 222 (1991).
- [68] P. Nozieres, *J. Phys. I France* **2**, 443 (1992).
- [69] D. Yudin, D. Hirschmeier, H. Hafermann, O. Eriksson, A. I. Lichtenstein, and M. I. Katsnelson, *Phys. Rev. Lett.* **112**, 070403 (2014).
- [70] G. E. Volovik, *JETP Lett.* **59**, 830 (1994).
- [71] A. A. Shashkin, V. T. Dolgoplov, J. W. Clark, V. R. Shaginyan, M. V. Zverev, and V. A. Khodel, *Phys. Rev. Lett.* **112**, 186402 (2014).
- [72] M. Tovmasyan, S. Peotta, L. Liang, P. Törmä, and S. D. Huber, *Phys. Rev. B* **98**, 134513 (2018).
- [73] C. Danieli, A. Andreanov, and S. Flach, *Phys. Rev. B* **102**, 041116(R) (2020).
- [74] Y. Kuno, T. Orito, and I. Ichinose, *New J. Phys.* **22**, 013032 (2020).
- [75] T. Orito, Y. Kuno, and I. Ichinose, *Phys. Rev. B* **101**, 224308 (2020).
- [76] A. Mielke, *J. Phys. A: Math. Gen.* **24**, 3311 (1991).
- [77] H. Tasaki, *Phys. Rev. Lett.* **69**, 1608 (1992).
- [78] A. Mielke, *J. Phys. A: Math. Gen.* **24**, L73 (1991).
- [79] A. Mielke and H. Tasaki, *Commun. Math. Phys.* **158**, 341 (1993).
- [80] H. Tasaki, *Eur. Phys. J. B* **64**, 365 (2008).
- [81] H. Tasaki, *Phys. Rev. Lett.* **73**, 1158 (1994).
- [82] M. Maksymenko, A. Honecker, R. Moessner, J. Richter, and O. Derzhko, *Phys. Rev. Lett.* **109**, 096404 (2012).
- [83] S. Peotta and P. Törmä, *Nat. Commun.* **6**, 8944 (2015).
- [84] A. Julku, S. Peotta, T. I. Vanhala, D.-H. Kim, and P. Törmä, *Phys. Rev. Lett.* **117**, 045303 (2016).
- [85] R. Mondaini, G. G. Batrouni, and B. Grémaud, *Phys. Rev. B* **98**, 155142 (2018).
- [86] G. E. Volovik, *JETP Lett.* **107**, 516 (2018).
- [87] A. Mielke, *J. Stat. Phys.* **171**, 679 (2018).
- [88] L. Capriotti and S. Sorella, *Phys. Rev. Lett.* **84**, 3173 (2000).
- [89] H. Mosadeq, F. Shahbazi, and S. A. Jafari, *J. Phys. Condens. Matter* **23**, 226006 (2011).
- [90] See Supplemental Material at <http://link.aps.org/supplemental/10.1103/PhysRevB.106.245109> for detailed calculation results of a configuration with bonding crosses at edges.
- [91] J. K. Asbóth, L. Oroszlány, and A. Pályi, A short course on topological insulators, *Lect. Notes Phys.* **919**, 1 (2016).
- [92] T. L. Hughes, E. Prodan, and B. A. Bernevig, *Phys. Rev. B* **83**, 245132 (2011).
- [93] G. van Miert, C. Ortix, and C. Morais Smith, *2D Mater.* **4**, 015023 (2017).
- [94] B. Perez-Gonzalez, M. Bello, A. Gomez-Leon, and G. Platero, *Phys. Rev. B* **99**, 035146 (2019).
- [95] Z.-Q. Jiao, S. Longhi, X.-W. Wang, J. Gao, W.-H. Zhou, Y. Wang, Y.-X. Fu, L. Wang, R.-J. Ren, L.-F. Qiao, and X.-M. Jin, *Phys. Rev. Lett.* **127**, 147401 (2021).